

See discussions, stats, and author profiles for this publication at: <https://www.researchgate.net/publication/251557046>

Pore pressure prediction from well logs: Methods, modifications, and new approaches

Article in *Earth-Science Reviews* · December 2011

DOI: 10.1016/j.earscirev.2011.06.001

CITATIONS

424

READS

26,445

1 author:



[Jon Jincai Zhang](#)

Hess Corporation

123 PUBLICATIONS 3,356 CITATIONS

SEE PROFILE



Pore pressure prediction from well logs: Methods, modifications, and new approaches

Jincai Zhang

Pore pressure prediction from well logs: methods, modifications, and new approaches

Jincai Zhang 张金才 原稿

Shell Exploration and Production Company, Houston, Texas, USA (Email: zhangjon@gmail.com)

Abstract

Pore pressures in most deep sedimentary formations are not hydrostatic; instead they are overpressured and elevated even to more than double of the hydrostatic pressure. If the abnormal pressures are not accurately predicted prior to drilling, catastrophic incidents, such as well blowouts and mud volcanoes, may take place. Pore pressure calculation in a hydraulically-connected formation is introduced. Fracture gradient prediction methods are reviewed, and the minimum and maximum fracture pressures are proposed. The commonly used empirical methods for abnormal pore pressure prediction from well logs are then reviewed in this paper. Eaton's resistivity and sonic methods are then adapted using depth-dependent normal compaction equations for pore pressure prediction in subsurface formations. The adapted methods provide a much easier way to handle normal compaction trendlines. In addition to the empirical methods, the theoretical pore pressure modeling is the fundamental to understand the mechanism of the abnormal pressure generation. A theoretical pore pressure-porosity model is proposed based on the primary overpressure generation mechanism - compaction disequilibrium and effective stress-porosity-compaction theory. Accordingly, pore pressure predictions from compressional velocity and sonic transit time are obtained using the new theoretical model. Case studies in deepwater oil wells illustrate how to improve pore pressure prediction in sedimentary formations.

Keywords

Abnormal pressure, pore pressure prediction, fracture pressure and fracture gradient, compaction disequilibrium, normal compaction trendline, porosity and overpressure, effective stress, velocity and transit time, resistivity, well logs, subsalt formations.

27
28
29
30
31
32
33
34
35
36
37
38
39
40
41
42
43
44
45
46
47
48
49
50
51
52
53
54
55
56
57
58

1. Introduction

1.1 Abnormal pore pressure and drilling incidents

Abnormal pore pressures, particularly overpressures, can greatly increase drilling non-productive time and cause serious drilling incidents (e.g., well blowouts, pressure kicks, fluid influx) if the abnormal pressures are not accurately predicted before drilling and while drilling. Study on 2,520 shelf gas wellbores drilled in the Gulf of Mexico shows that more than 24% non-productive time was associated with incidents of kicks, shallow water flow, gas flow and lost circulation (Dodson, 2004), which were caused by improper pore pressure and fracture gradient prediction. In deepwater (water depth > 3000 ft) of the Gulf of Mexico, incidents associated with pore pressure and wellbore instability took 5.6% of drilling time in non-subsalt wells, and 12.6% of drilling time in the subsalt wells (York et al., 2009). Furthermore, an investigation of drilling incidents shows that there are 48 kicks for 83 wells drilled in the deepwater Gulf of Mexico, and at least 21% of those kicks resulted in loss of all or part of the well (Holand and Skalle, 2001). Comprehensive analysis of 1,206 blowouts in the U.S.A. shows that there was one blowout incident for every 285 wells drilled (Skalle and Podio, 1998). The abnormally high pore pressures not only caused the kicks and blowouts, but also induced geologic disasters, such as mud volcano eruptions (Davies et al., 2007; Tingay et al., 2009). Therefore, accurate pore pressure prediction is of crucial importance for operators to reduce borehole trouble time and avoid drilling incidents.

Overpressures can be generated by many mechanism, such as compaction disequilibrium (under-compaction), hydrocarbon generation and gas cracking, aquathermal expansion, tectonic compression (lateral stress), mineral transformations (e.g., illitization), and osmosis, hydraulic head and hydrocarbon buoyancy (Gutierrez et al, 2006; Swarbrick and Osborne, 1998). In nearly all cases where compaction disequilibrium has been determined to be the primary cause of overpressuring, the age of the rocks is geologically young. Examples of areas where compaction disequilibrium is cited as the primary reason of abnormal pressure include the U.S. Gulf Coast, Alaska Cook Inlet; Beaufort Sea, Mackenzie Delta, North Sea, Adriatic Sea, Niger Delta, Mahakam Delta, the Nile Delta, Malay Basin, Eastern Venezuelan Basin (Trinidad) and the Potwar Plateau of Pakistan (Law and Spencer, 1998; Burrus, 1998; Heppard, et al., 1998; Powley, 1990; Nelson and Bird, 2005; Morley et al., 2011). In these areas, the abnormally pressured rocks are mainly located in Tertiary and late Mesozoic sedimentary formations, the depositional setting is dominantly deltaic, and the lithology is dominantly shale.

One of major reasons of abnormal pore pressure is caused by abnormal formation compaction (compaction disequilibrium or under-compaction). When sediments compact normally, formation porosity is reduced at the same time as pore fluid is expelled. During burial, increasing overburden pressure is the prime cause of fluid expulsion. If the sedimentation rate is slow, normal compaction occurs, i.e., equilibrium between increasing overburden and the reduction of pore fluid volume due to compaction (or ability to expel fluids) is maintained (Mouchet and Mitchell, 1989). This normal compaction generates hydrostatic pore pressure in the formation. Rapid burial, however, leads to faster expulsion of fluids in response to rapidly increasing overburden stress. When the sediments subside rapidly, or the formation has extremely low permeability, fluids in the sediments can only be partially expelled. The remained fluid in the pores of the sediments must support all or part of the weight of overly sediments, causing the pressure of pore fluids increases, i.e., abnormally high pore pressure. In this case porosity decreases less rapidly than it should be with depth, and formations are said to be under-compacted or in compaction disequilibrium. The overpressures generated by under-compaction in mudrock-dominated sequences may exhibit the following characteristic: the abnormal pore pressure change with depth is sub-parallel to the lithostatic (overburden) pressure gradient (Swarbrick et al., 2002). The compaction disequilibrium is often recognized by higher than expected porosities at a given depth and the porosities deviated from the normal porosity trend. However, the increase in porosity is not necessary caused merely by under-compaction and it could also be caused by other reasons, such as micro-fractures induced by hydrocarbon generation. Therefore, porosity increase and abnormal pressure may be caused by both under-compaction and hydrocarbon generation. Thus, by knowing the normal porosity trend and measured formation porosities (can be obtained from well log data), one can calculate the formation pore pressure.

81

82 **1.2. Pore pressure and pore pressure gradient**

83

84 Pore pressure is one of the most important parameters for drilling plan and for geomechanical and
85 geological analyses. Pore pressures are the fluid pressures in the pore spaces in the porous formations.
86 Pore pressure varies from hydrostatic pressure, to severe overpressure (48% to 95% of the overburden
87 stress). If the pore pressure is lower or higher than the hydrostatic pressure (normal pore pressure), it is
88 abnormal pore pressure. When pore pressure exceeds the normal pressure, it is overpressure.

89

90 The fundamental theory for pore pressure prediction is based on Terzaghi's and Biot's effective stress law (Terzaghi et al., 1996; Biot, 1941). This theory indicates that pore pressure in the formation is a

function of total stress (or overburden stress) and effective stress. The overburden stress, effective vertical stress and pore pressure can be expressed in the following form:

$$p = (\sigma_v - \sigma_e) / \alpha \quad (1)$$

where p is the pore pressure; σ_v is the overburden stress; σ_e is the vertical effective stress; α is the Biot effective stress coefficient. It is conventionally assumed $\alpha = 1$ in geopressure community.

Pore pressure can be calculated from Eq. 1 when one knows overburden and effective stresses. Overburden stress can be easily obtained from bulk density logs, while effective stress can be correlated to well log data, such as resistivity, sonic travel time/velocity, bulk density and drilling parameters (e.g., D exponent). Fig. 1 demonstrates the hydrostatic pressure, formation pore pressure, overburden stress and vertical effective stress with the true vertical depth (TVD) in a typical oil and gas exploration well. The pore pressure profile with depth in this field is similar to many geologically young sedimentary basins where overpressure is encountered at depth. At relatively shallow depths (less than 2,000 m), pore pressure is hydrostatic, indicating that a continuous, interconnected column of pore fluid extends from the surface to that depth. Deeper than 2,000 m the overpressure starts, and pore pressure increases with depth rapidly, implying that the deeper formations are hydraulically isolated from shallower ones. By 3,800 m, pore pressure reaches to a value close to the overburden stress, a condition referred to as hard overpressure. The effective stress is conventionally defined to be the subtraction of pore pressure from overburden stress (refer to Eq. 1), as shown in Fig. 1. The increase in overpressure causes reduction in the effective stress.

The pore pressure gradient is more practically used in drilling engineering, because the gradients are more convenient to be used for determining mud weight (or mud density), as shown in Fig. 2. The pore pressure gradient at a given depth is the pore pressure divided by the true vertical depth. The mud weight should be appropriately selected based on pore pressure gradient, wellbore stability and fracture gradient prior to setting and cementing a casing. The drilling fluid (mud) is applied in the form of mud pressure to support the wellbore walls for preventing influx and wellbore collapse during drilling. To avoid fluid influx, kicks and wellbore instability in an open hole section, a heavier mud pressure than the pore pressure is needed. However, when mud weight is higher than the fracture gradient of the drilling section, it may fracture the formation, causing mud losses or even lost circulation. To prevent wellbore from hydraulic fracturing by the high mud weight, as needed where there is overpressure, casing needs to be set to protect the overlying formations from fracturing, as illustrated in Fig. 2.

Pressure gradients and mud weight are expressed in the metric unit, g/cm^3 (also called specific gravity or SG) in Fig. 2. Pressure gradients and mud weight are often reported in English or American

unit in the oil and gas industry. The pressure gradient conversions between American and metric units are listed in Table 1.

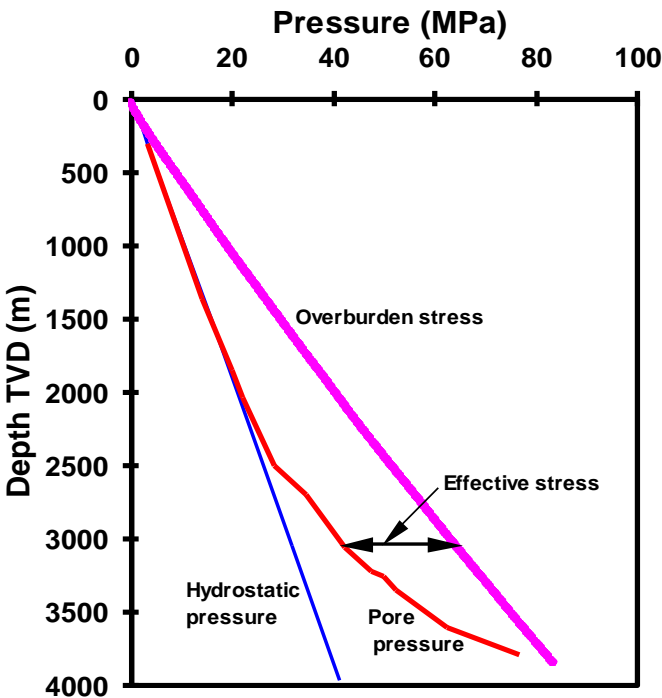


Fig. 1. Hydrostatic pressure, pore pressure, overburden stress, and effective stress in a borehole.

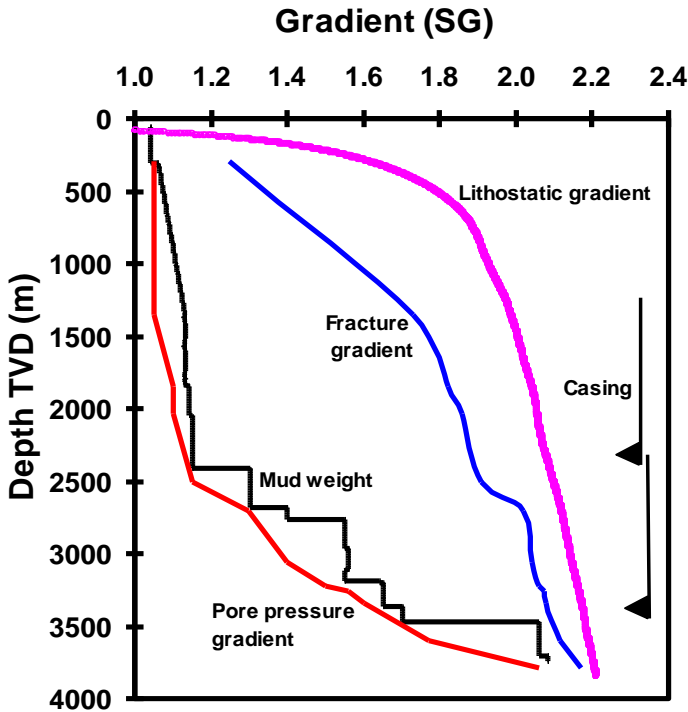


Fig. 2. Pore pressure gradient, fracture gradient, overburden stress gradient (lithostatic gradient), mud

weight, and casing shoes with depth. In this figure the pore pressure and overburden gradients are converted from the pore pressure and overburden stress plotted in Fig. 1.

Table 1. Conversions of pressure gradients in American and metric units.

Conversions	Conversions
$1 \text{ g/cm}^3 = 9.81 \text{ MPa/km}$	$1 \text{ ppg} = 0.051948 \text{ psi/ft}$
$1 \text{ g/cm}^3 = 0.00981 \text{ MPa/m}$	$1 \text{ ppg} = 0.12 \text{ g/cm}^3$
$1 \text{ g/cm}^3 = 1 \text{ SG}$	$1 \text{ ppg} = 0.12 \text{ SG}$
$1 \text{ MPa/km} = 0.102 \text{ SG} = 0.102 \text{ g/cm}^3$	$1 \text{ ppg} = 1.177 \text{ MPa/km}$
$1 \text{ MPa/km} = 1 \text{ kPa/m}$	$1 \text{ ppg} = 1.177 \text{ kPa/m}$
$1 \text{ g/cm}^3 = 8.345 \text{ ppg}$	$1 \text{ psi/ft} = 19.25 \text{ ppg}$
$1 \text{ g/cm}^3 = 0.4335 \text{ psi/ft}$	$1 \text{ psi/ft} = 2.31 \text{ g/cm}^3$
$1 \text{ SG} = 8.345 \text{ ppg}$	$1 \text{ psi/ft} = 22.66 \text{ MPa/km}$
$1 \text{ SG} = 0.4335 \text{ psi/ft}$	$1 \text{ psi/ft} = 2.31 \text{ SG}$
$1 \text{ SG} = 62.428 \text{ pcf (lb/ft}^3\text{)}$	$1 \text{ ppg} = 7.4805 \text{ pcf}$

Pore pressure analyses include three aspects: pre-drill pore pressure prediction, pore pressure prediction while drilling and post-well pore pressure analysis. The pre-drill pore pressure can be predicted by using the seismic interval velocity data in the planned well location as well as using geological, well logging and drilling data in the offset wells. The pore pressure prediction while drilling mainly uses the logging while drilling (LWD), measurement while drilling (MWD), drilling parameters, and mud logging data for analyses. The post-well analysis is to analyze pore pressures in the drilled wells using all available data to build pore pressure model, which can be used for pre-drill pore pressure predictions in the future wells.

1.3. Fracture pressure and fracture gradient

Fracture pressure is the pressure required to fracture the formation and cause mud loss from wellbore into the induced fracture. Fracture gradient can be obtained by dividing the true vertical depth from the fracture pressure. Fracture gradient is the maximum mud weight; therefore, it is an important parameter for mud weight design in both drilling planning stage and while drilling. If mud weight is higher than the formation fracture gradient, then the wellbore will have tensile failure (be fractured), causing losses of drilling mud or even lost circulation. Fracture pressure can be measured directly from downhole leak-off

test (LOT). There are several approaches to calculate fracture gradient. The following two methods are commonly used in the drilling industry; i.e., the minimum stress method and tensile failure method.

1.3.1. Minimum stress for lower bound of fracture gradient

The minimum stress method does not include any accommodation for the tensile strength of the rock, rather it represents the pressure required to open and extend a pre-existing fracture in the formation. Therefore, the minimum stress represents the lower bound of fracture pressure. The minimum stress is the minimum principal in-situ stress and typically equal to the fracture closure pressure, which can be observed on the decline curve of a leak-off test following the breakdown pressure (Zhang et al., 2008). The minimum stress method, as shown in the following, is similar to the methods proposed by Hubbert and Willis (1957), Eaton (1968) and Daines (1982).

$$\sigma_{\min} = \frac{\nu}{1-\nu}(\sigma_v - p) + p \quad (2)$$

where σ_{\min} is the minimum in-situ stress or the lower bound of fracture pressure; ν is the Poisson's ratio, can be obtained from the compressional and shear velocities (v_p and v_s), and $\nu = \frac{\frac{1}{2}(v_p/v_s)^2 - 1}{(v_p/v_s)^2 - 1}$.

When the open fractures exist in the formation, the fracture gradient may be even lower than the minimum stress.

Matthews and Kelly (1967) introduced a variable of effective stress coefficient for fracture gradient prediction:

$$P_{FG} = K_0(OBG - P_{pg}) + P_{pg} \quad (3)$$

where P_{FG} is the formation fracture gradient; P_{pg} is the formation pore pressure gradient; OBG is the overburden stress gradient; K_0 is the effective stress coefficient, $K_0 = \sigma_{\min}'/\sigma_v'$; σ_{\min}' is the minimum effective in-situ stress; σ_v' is the maximum effective in-situ stress or effective overburden stress. In this method the values of K_0 were established on the basis of fracture threshold values derived empirically in the field. The K_0 can be obtained from LOT and regional experiences.

1.3.2. Formation breakdown pressure for upper bound of fracture gradient

For intact formations, only after a tensile failure appeared in the wellbore can mud loss occur. In this case, fracture pressure/gradient can be calculated from Kirsch's solution when the minimum tangential stress is equal to the tensile strength (Haimson and Fairhurst, 1970; Zhang and Roegiers, 2010). This fracture

pressure is the fracture breakdown pressure in LOT (Zhang et al., 2008). For a vertical well, the fracture breakdown pressure or the upper bound of fracture pressure can be expressed as follows:

$$P_{FP\max} = 3\sigma_{\min} - \sigma_H - p - \sigma_T + T_0 \quad (4)$$

where $P_{FP\max}$ is the upper bound of fracture pressure; σ_H is the maximum horizontal stress; σ_{\min} is the minimum horizontal stress or minimum in-situ stress; σ_T is the thermal stress induced by the difference between the mud temperature and the formation temperature, and T_0 is the tensile strength of the rock.

Neglecting tensile strength and temperature effect and assuming σ_H is approximately equal to σ_{\min} , Eq. 4 can be simplified to the following form:

$$P_{FP\max} = 2\sigma_{\min} - p \quad (5)$$

Substituting Eq. 2 into Eq. 5, the upper bound of fracture pressure can be expressed as:

$$P_{FP\max} = \frac{2\nu}{1-\nu}(\sigma_v - p) + p \quad (6)$$

Compared this upper bound of fracture pressure (Eq. 6) to the lower bound of fracture pressure (Eq. 2), the only difference is the constant in front of effective vertical stress ($\sigma_v - p$). This upper bound of fracture gradient can be considered as the maximum fracture gradient, or the bound of lost circulation (Zhang et al., 2008).

Therefore, the average of the lower bound and upper bound of fracture pressures can be used as the most likely fracture pressure, .i.e.:

$$P_{FP} = \frac{3\nu}{2(1-\nu)}(\sigma_v - p) + p \quad (7)$$

where P_{FP} is the most likely fracture pressure.

1.4. Pore pressure in a hydraulically connected formation

Before introducing methods of well-log-based pore pressure prediction, it should be noted that the methods are based on the shale (mudrock) properties, and the pore pressures obtained from these methods are the pressures in shales. For the pressures in sandstones, limestones or other permeable formations, the pore pressure can be obtained by either assuming that the shale pressure is equal to the sandstone pressure, or using centroid method (Dickinson, 1953; Traugott, 1997; Bowers, 2001) and using lateral flow model (Yardley and Swarbrick, 2000; Meng et al., 2011) to do calculation. In either centroid method or lateral flow model, the principle is similar and based on the following equation (Eq. 8) for a hydraulically connected and fully saturated formation.

Where a laterally extensive inclined aquifer or a hydrocarbon-bearing formation exists, deep overpressured regions are connected to shallower regions by a permeable pathway. Fluid flow along such an inclined formation can cause pore pressures at the crest of a structure to increase. The pressures in a hydraulically connected formation can be calculated based on the difference in the heights of fluid columns, i.e.:

$$p_2 = p_1 + \rho_f g(Z_2 - Z_1) \quad (8)$$

where p_1 is the formation fluid pressure at depth of Z_1 ; p_2 is the formation fluid pressure at depth of Z_2 ; ρ_f is the in-situ fluid density; g is the acceleration of gravity.

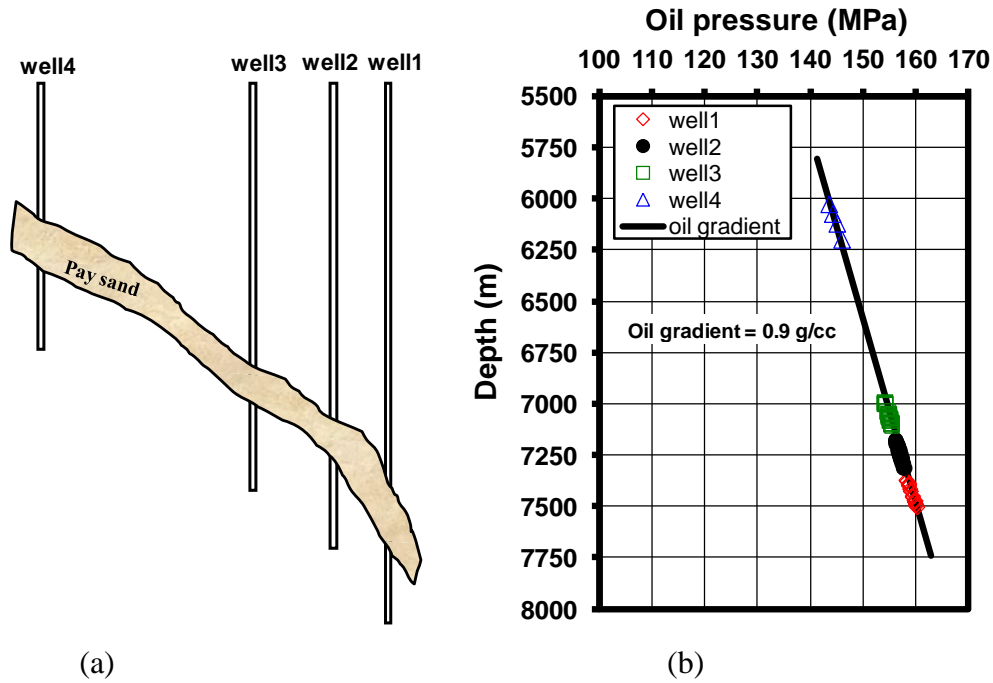


Fig. 3. Schematic cross section (left) showing four wells in a hydraulically connected oil-bearing sandstone compartment and the fluid pressures in different wells (right). Measured fluid pressures (dots) in these wells match the calculated pore pressures (line) with an oil gradient of 0.9 g/cm^3 .

Therefore, for a permeable aquifer or hydrocarbon-bearing formation if we know the formation pressure at a certain depth, then the pressures at other depths can be obtained from Eq. 8. The calculation and principle is relatively simple. However, to perform this calculation, we need to know the connectivity and extension area of the formation. In other words, we need to distinguish each individual fluid compartment and seal, which can be determined from regional geology, well logging data and drilling data (Powley, 1990). Fig. 3 shows an example of calculating formation pressure in an oil-bearing sandstone using the fluid flow model (Eq. 8). When the formation pressure and fluid density in Well 1 are

known, we can calculate the pressures in other wells using Eq. 8. When the formation is hydraulically connected and saturated with the same fluid, the formation pressures in the four wells should follow a single fluid gradient. Fig. 3 demonstrates that Eq. 8 gives an excellent prediction. Therefore, when the geologic structure, fluid pressure and density in a well are known, the fluid pressures in other wells located in a hydraulically connected formation can be fairly predicted. It should be noted that the permeability magnitude and its variation may affect the hydraulic connectivity of a formation. For extremely low permeable formations (e.g., shale gas formation), the applicability of Eq. 8 may be limited.

Pore pressure gradient is different in a formation when it is saturated with different fluids. In each fluid column, the pore pressure can be calculated using Eq. 8 with the density of the fluid saturated in this column. Fig. 4 show a hydraulically connected formation filled with gas, oil and water/brine. If we know the fluid pressure at a depth, fluid densities, and depths of water-oil contact (WOC) and oil-gas contact (OGC), then we can use Eq. 8 to calculate the pressures at other depths. Therefore, in Location A (the crest) the gas pressure can be expressed as follows:

$$p_A = p_B + \rho_g g(Z_A - Z_B)$$

where ρ_g is the in-situ gas density; p_B is the pore pressure in Location B; p_A is the pore pressure in Location A.

In Location B (oil-gas contact), the oil pressure can be obtained from the following equation:

$$p_B = p_C + \rho_o g(Z_B - Z_C)$$

where ρ_o is the in-situ oil density; p_C is the pore pressure in Location C; p_B is the pore pressure in Location B.

If the formation is only saturated with water, then the pressure in Location A is:

$$p_{wA} = p_C + \rho_w g(Z_A - Z_C)$$

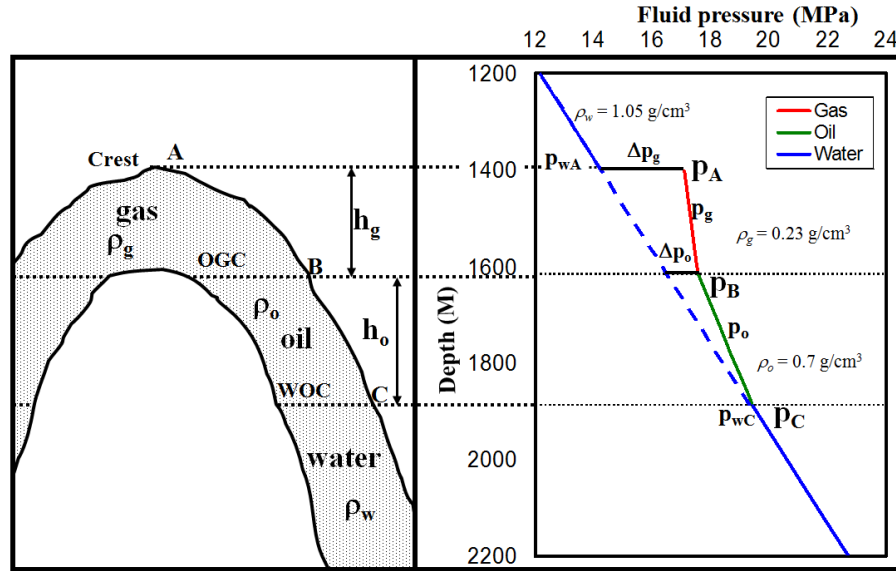
Compared the pressure (p_A) in the crest to the water/brine pressure (p_{wA}) at the same depth, the pore pressure increment induced by oil and gas column in the crest (location A in Fig. 4) can be expressed in the following form (i.e., $\Delta p_{og} = p_A - p_{wA}$):

$$\Delta p_{og} = (\rho_w - \rho_o)gh_o + (\rho_w - \rho_g)gh_g \quad (9)$$

where Δp_{og} is the pore pressure increment induced by the oil and gas columns; ρ_w is the in-situ water/brine density; h_g is the height of gas column; h_o is the height of the oil column.

It should be noted that gas density is highly dependent on pressure. Therefore, the in-situ gas density should be used for the calculations. Normally, the gas column height is not very large; hence, in the aforementioned equations gas density is assumed to be a constant value.

264 This pore pressure elevation (Δp_{og} in Eq. 9) is caused by hydrocarbon buoyancy effect due to
 265 density contrasts between hydrocarbon and brine. The pressure elevation due to the difference in densities
 266 gradually decreases from the maximum value at the top of the reservoir to zero at the water and
 267 hydrocarbon contact.



268
 269 **Fig. 4.** A schematic reservoir saturated with gas, oil and water (left) and pore pressure elevated by oil and
 270 gas columns and density contrast between water and oil, gas in a reservoir. This density contrast causes
 271 pore pressure increase in Location A compared to the one caused only by water/brine gradient. The right
 272 figure shows pore pressure elevated by hydrocarbon columns in a hydraulically connected formation.

274 2. Review of some methods of pore pressure prediction

276 Hottmann and Johnson (1965) were probably the first ones to make pore pressure prediction from shale
 277 properties derived from well log data (acoustic travel time/velocity and resistivity). They indicated that
 278 porosity decreases as a function of depth from analyzing acoustic travel time in Miocene and Oligocene
 279 shales in Upper Texas and Southern Louisiana Gulf Coast. This trend represents the “normal compaction
 280 trend” as a function of burial depth, and fluid pressure exhibited within this normal trend is the
 281 hydrostatic. If intervals of abnormal compaction are penetrated, the resulting data points diverge from the
 282 normal compaction trend. They contended that porosity or transit time in shale is abnormally high relative
 283 to its depth if the fluid pressure is abnormally high.

284 Analyzing the data presented by Hottmann and Johnson (1965), Gardner et al. (1974) proposed an
 285 equation that can be written in the following form to predict pore pressure:

$$p_f = \sigma_v - \frac{(\alpha_v - \beta)(A_1 - B_1 \ln \Delta t)^3}{Z^2} \quad (4)$$

where p_f is the formation fluid pressure (psi); σ_v is expressed in psi; α_v is the normal overburden stress gradient (psi/ft); β is the normal fluid pressure gradient (psi/ft); Z is the depth (ft); Δt is the sonic transit time (μ s/ft); A and B are the constants, $A_1 = 82776$ and $B_1 = 15695$.

Later on, many empirical equations for pore pressure prediction were presented based on resistivity, sonic transit time (interval velocity) and other well logging data. The following sections only introduce some commonly used methods of pore pressure prediction based on the shale properties.

2.1. Pore pressure prediction from resistivity

In young sedimentary basins where under-compaction is the major cause of overpressure, e.g., the Gulf of Mexico, North Sea, the well-log-based resistivity method can fairly predict pore pressure. Eaton (1972, 1975) presented the following equation to predict pore pressure gradient in shales using resistivity log:

$$P_{pg} = OBG - (OBG - P_{ng}) \left(\frac{R}{R_n} \right)^n \quad (5)$$

where P_{pg} is the formation pore pressure gradient; OBG is the overburden stress gradient; P_{ng} is the hydrostatic pore pressure gradient (normally 0.45 psi/ft or 1.03 MPa/km, dependent on water salinity); R is the shale resistivity obtained from well logging; R_n is the shale resistivity at the normal (hydrostatic) pressure; n is the exponent varied from 0.6-1.5, and normally $n = 1.2$.

Eaton's resistivity method is applicable in pore pressure prediction, particularly for young sedimentary basins, if the normal shale resistivity is properly determined (e.g., Lang et al., 2011). One approach is to assume that the normal shale resistivity is a constant. The other approach includes to accurately determine the normal compaction trendline, which will be presented in Section 3.1 to address this issue.

2.2. Pore pressure prediction from interval velocity and transit time

2.2.1. Eaton's Method

Eaton (1975) presented the following empirical equation for pore pressure gradient prediction from sonic compressional transit time:

$$P_{pg} = OBG - (OBG - P_{ng}) \left(\frac{\Delta t_n}{\Delta t} \right)^3 \quad (6)$$

where Δt_n is the sonic transit time or slowness in shales at the normal pressure; Δt is the sonic transit time in shales obtained from well logging, and it can also be derived from seismic interval velocity.

This method is applicable in some petroleum basins, but it does not consider unloading effects. This limits its application in geologically complicated area, such as formations with uplifts. To apply this method, one needs to determine the normal transit time (Δt_n).

321

322 **2.2.2 Bowers' Method**

Bowers (1995) calculated the effective stresses from measured pore pressure data of the shale and overburden stresses (using Eq. 1) and analyzed the corresponded sonic interval velocities from well logging data in the Gulf of Mexico slope. He proposed that the sonic velocity and effective stress have a power relationship as follows:

$$v_p = v_{ml} + A \sigma_e^B \quad (7)$$

where v_p is the compressional velocity at a given depth; v_{ml} is the compressional velocity in the mudline (i.e., the sea floor or the ground surface, normally $v_{ml} \approx 5000$ ft/s, or 1520 m/s); A and B are the parameters calibrated with offset velocity versus effective stress data.

Rearranging Eq. 7 and considering $\sigma_e = \sigma_v - p$, the pore pressure can be obtained from the velocity as described in Eq. 7, as:

$$p = \sigma_v - \left(\frac{v_p - v_{ml}}{A} \right)^{\frac{1}{B}} \quad (8)$$

For Gulf of Mexico wells, $A = 10 - 20$ and $B = 0.7 - 0.75$ in the English units (with p , σ_v in psi and v_p , v_{ml} in ft/s). Eq. 8 can also be written in terms of transit time simply by substituting $10^6/\Delta t$ for v_p and $10^6/\Delta t_{ml}$ for v_{ml} :

$$p = \sigma_v - \left(\frac{10^6 \left(\frac{1}{\Delta t} - \frac{1}{\Delta t_{ml}} \right)}{A} \right)^{\frac{1}{B}} \quad (9)$$

where Δt_{ml} is the compressional transit time in the mudline, normally $\Delta t_{ml} = 200$ μ s/ft or 660 μ s/m.

The effective stress and compressional velocity do not follow the loading curve if formation uplift or unloading occurs, and a higher than the velocity in the loading curve appears at the same effective

stress. Bowers (1995) proposed the following empirical relation to account for the effect of unloading curves:

$$v_p = v_{ml} + A \left[\sigma_{\max} (\sigma_e / \sigma_{\max})^{1/U} \right]^B \quad (10)$$

where σ_e , v_p , v_{ml} , A and B are as before; U is the uplift parameter; and

$$\sigma_{\max} = \left(\frac{v_{\max} - v_{ml}}{A} \right)^{\frac{1}{B}}$$

where σ_{\max} and v_{\max} are the estimates of the effective stress and velocity at the onset unloading. In absence of major lithology changes, v_{\max} is usually set equal to the velocity at the start of the velocity reversal.

Rearranging Eq. 10 the pore pressure can be obtained for the unloading case:

$$p_{ulo} = \sigma_v - \left(\frac{v_p - v_{ml}}{A} \right)^{\frac{U}{B}} (\sigma_{\max})^{1-U} \quad (11)$$

where p_{ulo} is the pore pressure in the unloading case.

Bowers' method is applicable to many petroleum basins (e.g., the Gulf of Mexico). However, this method overestimated pore pressure when shallow formation is poorly- or un-consolidated, because the velocity in such a formation is very slow.

2.2.3 Miller's Method

The Miller sonic method describes a relationship between velocity and effective stress that can be used to relate sonic/seismic transit time to formation pore pressure. In Miller's sonic method an input parameter "maximum velocity depth", d_{\max} , controls whether unloading has occurred or not. If d_{\max} is less than the depth (Z), unloading has not occurred, the pore pressure can be obtained from the following equation (Zhang et al., 2008):

$$p = \sigma_v - \frac{1}{\lambda} \ln \left(\frac{v_m - v_{ml}}{v_m - v_p} \right) \quad (12)$$

where v_m is the sonic interval velocity in the matrix of the shale (asymptotic travel time at infinite effective stress, $v_m = 14000$ - 16000 ft/s); v_p is the compressional velocity at a given depth; λ is the empirical parameter defining the rate of increase in velocity with effective stress (normally 0.00025); d_{\max} is the depth at which the unloading has occurred.

If $d_{\max} \geq Z$, then unloading behavior is assumed, the pore pressure in the unloading case is calculated from the following equation:

$$p_{ulo} = \sigma_v - \frac{1}{\lambda} \ln \left[a_m \left(1 - \frac{v_p - v_{ulo}}{v_m - v_{ml}} \right) \right] \quad (13)$$

where a_m is the ratio of slopes of the virgin (loading) and unloading velocities in the effective stress curves σ_{ul} (normally $a_m = 1.8$) and $a_m = v_p/v_{ulo}$; σ_{ul} is the effective stress from unloading of the sediment; v_{ulo} is the velocity where unloading begins.

2.2.4 Tau model

A velocity-dependent pore pressure prediction method was proposed by Shell through introducing a “Tau” variable into the effective stress equation (Lopez et al., 2004; Gutierrez et al, 2006):

$$\sigma_e = A_s \tau^{B_s} \quad (14)$$

where A_s and B_s are the fitting constants; τ is the Tau variable, and $\tau = (C - \Delta t)/(\Delta t - D)$; Δt is the compressional transit time either from sonic log or seismic velocity; C is the constant related to the mudline transit time (normally $C = 200 \mu\text{s/ft}$); and D is the constant related to the matrix transit time (normally $D = 50 \mu\text{s/ft}$).

Then, the pore pressure can be calculated from Eq. 14 using Eq. 1, i.e.:

$$p = \sigma_v - A_s \left(\frac{C - \Delta t}{\Delta t - D} \right)^{B_s} \quad (15)$$

The best fitting parameters in the Gulf of Mexico are $A_s = 1989.6$ and $B_s = 0.904$ (Gutierrez et al, 2006).

Tau model and Miller’s method are similar to Bowers’ method. The advantage of Miller’s method and Tau model is that both the effects of the matrix and mudline velocities are considered on pore pressure prediction.

3. Adapted Eaton’s methods with depth-dependent normal compaction trendlines

3.1. Eaton’s resistivity method with depth-dependent normal compaction trendline

In Eaton’s original equation, it is difficult to determine the normal shale resistivity or the shale resistivity in the condition of hydrostatic pore pressure. One approach is to assume that the normal shale resistivity is a constant. However, the normal resistivity (R_n) is not a constant in most cases, but a function of the

399 burial depth, as shown in Fig. 5. Thus normal compaction trendline needs to be determined for pore
 400 pressure prediction.

401 Based on the relationship of measured resistivity and burial depth in the formations with normal
 402 pressures, the following equation of the normal compaction trend of resistivity can be used (refer to Fig.
 403 5):

404 $\ln R_n = \ln R_0 + bZ$

405 or

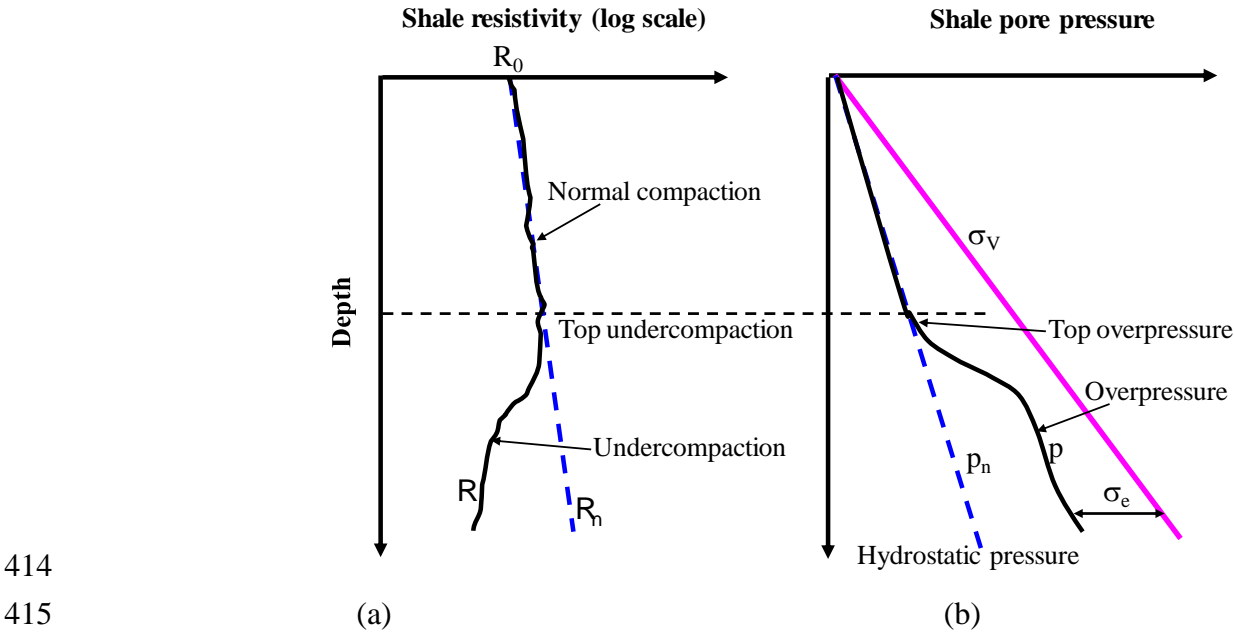
406 $R_n = R_0 e^{bZ}$ (16)

407 where R_n is the shale resistivity in the normal compaction condition; R_0 is the shale resistivity in the
 408 mudline; b is the constant; Z is the depth below the mudline.

409 Substituting Eq. 16 into Eq. 5, the Eaton's resistivity equation can be expressed in the following
 410 form:

411 $P_{pg} = OBG - (OBG - P_{ng}) \left(\frac{R}{R_0 e^{bZ}} \right)^n$ (17)

412 where: R is the measured shale resistivity at depth of Z ; R_0 is the normal compaction shale resistivity in
 413 the mudline; b is the slope of logarithmic resistivity normal compaction trendline.



414
 415 **Fig. 5.** Schematic resistivity (a) and pore pressure (b) in an undercompacted basin. The inclined line in (a)
 416 represents the resistivity in normally compacted formation (normal resistivity, R_n). In the under-
 417 compacted section the resistivity (R) reversal occurs, corresponding an overpressured formation in (b). In
 418 the under-compacted/overpressured section, resistivity is lower than that in the normal compaction
 419

420 trendline (R_n). In the figure, σ_v = lithostatic or overburden stress; σ_e = the effective vertical stress; p_n =
421 normal pore pressure; p = pore pressure.

422

423 A case study is examined to verify the adapted Eaton's resistivity method with depth dependence.
424 The studied basin is located in a deepwater field in Green Canyon of the Gulf of Mexico, U.S.A. The
425 water depth is 5000 ft, and the Tertiary formations are mainly shales (mudstones) with some sandstones.
426 The target reservoir is located in the Miocene sandstones. Several offset wells are analyzed to examine
427 pore pressures in this field. Fig. 6 shows the pore pressure calculation in an oil well from the modified
428 Eaton's resistivity method in this basin. Prior to the pore pressure calculation, the normal resistivity
429 compaction trend is firstly analyzed based on Eq. 16, as shown in Fig. 6.a. With calibration of the
430 measured pore pressure data, the normal compaction trendline is obtained with the following parameters
431 in this basin: $R_0 = 1.28$ ohmm, $b = 0.000034$. Pore pressure calculated from the adapted Eaton's method
432 (Eq. 17 with $n = 1.2$, $P_{ng} = 8.7$ ppg) is compared to the measured pore pressure from the repeat formation
433 tests (RFT) and mud weight. Fig. 6 indicates that the formation is in normal compaction when depth is
434 less than 4900 ft below the sea floor. Deeper than this depth (from 4900-7600 ft), the formation is slightly
435 under-compacted with a lower resistivity than the normal compaction trend (Fig. 6.a), implying that the
436 pore pressure increases, as shown in Fig. 6.b. From 7600-13000 ft, the formation is further under-
437 compacted and more elevated pore pressures exist. Fig. 6 demonstrates that the adapted Eaton's resistivity
438 method gives a fairly good result in pore pressure calculation.

439 It should be noted that the pore pressure in the formation near the wellbore is affected by drilling-
440 induced stresses (Zhang and Roegiers, 2005). Therefore, in order to obtain the formation pore pressure the
441 deep resistivity is needed for the pore pressure calculation.

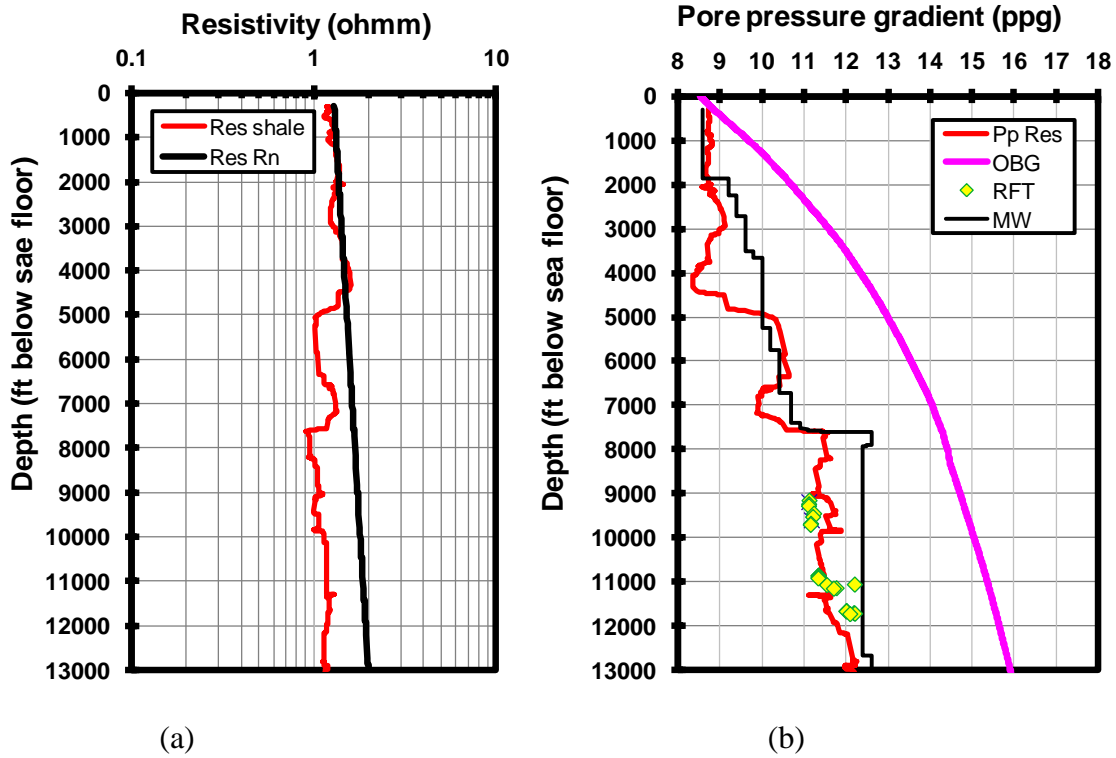


Fig. 6. Pore pressure calculated by adapted Eaton's resistivity method with depth-dependent compaction trendline in a deepwater post-well analysis in the Gulf of Mexico. The left figure (a) plots the resistivity in shale and the normal resistivity calculated from Eq. 16, and the resistivity is plotted in logarithmic scale. The right figure (b) shows the overburden stress gradient (OBG), mud weight used while drilling (MW), measured pore pressure gradient (RFT) and pore pressure gradient (Pp Res) calculated from resistivity using Eq. 17.

3.2. Eaton's velocity method with depth-dependent normal compaction trendline

Slotnick (1936) recognized that the compressional velocity is a function of depth, i.e., velocity increases with depth in the subsurface formations. Therefore, the normal compaction trendline of travel time should be a function of depth. The oldest and simplest normal compaction trend of seismic velocity is a linear relationship given by Slotnick (1936) in the following form:

$$v = v_0 + kZ \quad (18)$$

where v is the seismic velocity at depth of Z ; v_0 is the velocity in the ground surface or at the sea floor; k is a constant.

Sayers et al. (2002) used this relationship as the normally pressured velocity for pore pressure prediction. A normal compaction trend for shale acoustic travel time with depth in the Carnarvon Basin

was established by fitting an exponential relationship to averaged acoustic travel times from 17 normally pressured wells (van Ruth et al., 2004):

$$\Delta t_n = 225 + 391e^{-0.00103Z} \quad (19)$$

where Δt_n is the acoustic transit time from the normal compaction trend at the depth of investigation ($\mu\text{s}/\text{m}$); Z is in meters.

A similar relationship was used for a petroleum basin in Brunei (Tingay et al., 2009):

$$\Delta t_n = 176.5 + 461.5e^{-0.0007Z}. \quad (20)$$

Based on the data of the measured sonic transit time in the formations with normal pore pressures, as illustrated in Fig. 7, the following general relationship of the normal compaction trend of the transit time is proposed (refer to Appendix B for derivations):

$$\Delta t_n = \Delta t_m + (\Delta t_{ml} - \Delta t_m)e^{-cZ} \quad (21)$$

where Δt_m is the compressional transit time in the shale matrix (with zero porosity); Δt_{ml} is the mudline transit time; c is the constant.

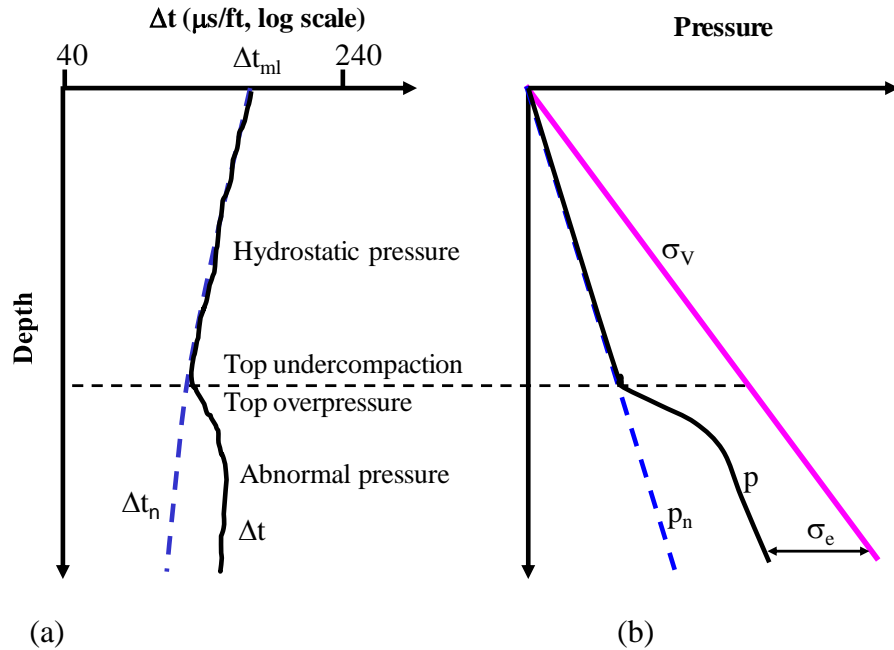


Fig. 7. Schematic plots showing sonic transit time (Δt) measured in shale, the normal compaction trend of the transit time in the normal pressure condition (Δt_n) and the pore pressure response to the transit time (Δt).

Substituting Eq. 21 into Eq. 6, the modified Eaton's sonic equation can be expressed in the following form:

$$P_{pg} = OBG - (OBG - P_{ng}) \left(\frac{\Delta t_m + (\Delta t_{ml} - \Delta t_m) e^{-cZ}}{\Delta t} \right)^3 \quad (23)$$

The same case study, as presented in Section 3.1, is used to examine the adapted Eaton's sonic transit time/velocity method. Fig. 8 shows the determination of normal compaction trend of sonic transit time from Eq. 21 and pore pressure calculation using the Eaton's sonic method with depth-dependent compaction trendline from Eq. 23. By calibrating the measured pore pressure data, the normal compaction trend is determined from Eq. 21 with the following parameters: $\Delta t_m = 70 \mu\text{s/ft}$, $\Delta t_{ml} = 200 \mu\text{s/ft}$ and $c = 0.000245$. Compared to measured pore pressure data the pore pressure calculation from Eq. 23 (Fig. 8) gives a very good result.

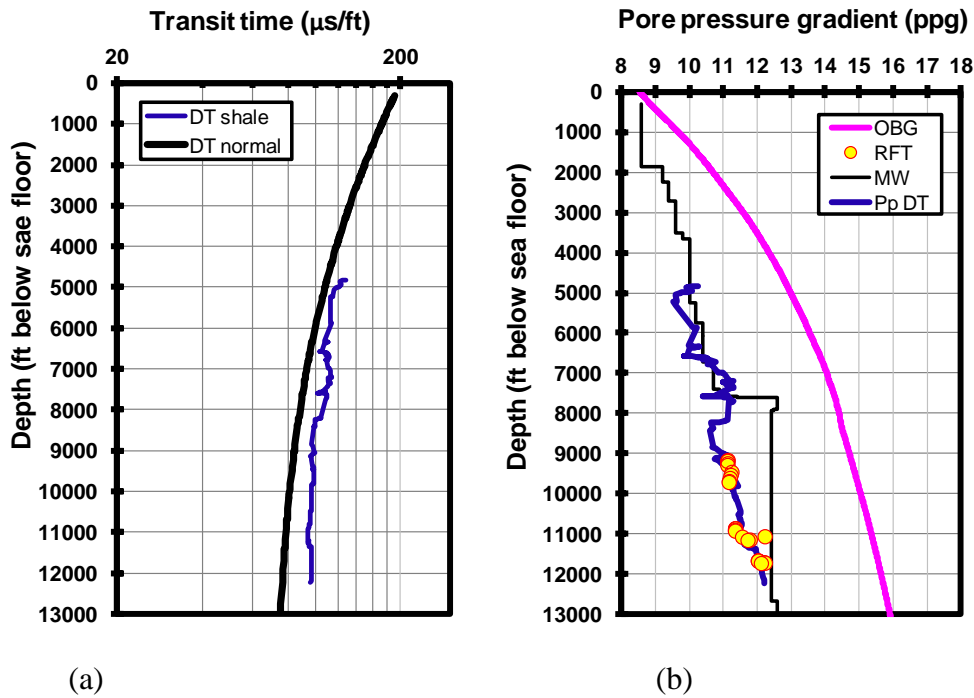


Fig. 8. Pore pressure calculated by adapted Eaton's sonic velocity method with depth-dependent compaction trendline in a deepwater well in the Gulf of Mexico. The left figure plots the sonic transit time in shale and the normal transit time calculated from Eq. 21, and the transit time is plotted in logarithmic scale. The right figure shows the overburden gradient (OBG), mud weight used while drilling (MW), measured pore pressure (RFT) and pore pressure gradient (Pp DT) calculated from sonic transit time using Eq. 23.

4. New theoretical models of pore pressure prediction

4.1. Pore pressure prediction from porosity

503

504 As introduced before, the under-compaction is the primary reason to cause formation overpressured,
505 which occur primarily in rapidly subsiding basins and in rocks with low permeability. The indicators of
506 under-compaction are higher pore pressure and larger formation porosity than those in the normal
507 compaction condition. It is commonly accepted that porosity decreases exponentially as depth increases in
508 normally compacted formations (e.g., Athy, 1930):

509
$$\phi = \phi_0 e^{-cZ} \quad (24)$$

510 where ϕ is porosity; ϕ_0 is the porosity in the mudline; Z is the true vertical depth below the mudline; c is
511 the compaction constant in 1/m or 1/ft.

512 The same relationship exists in porosity and effective stress (e.g., Dutta, 2002; Flemings et al.,
513 2002; Peng and Zhang, 2007).

514
$$\phi = \phi_0 e^{-a\sigma_e} \quad (25)$$

515 where a is the stress compaction constant in 1/psi or 1/MPa.

516 As discussed previously, porosity is an indicator (a function) of effective stress and pore pressure,
517 particularly for the overpressures generated from under-compaction and hydrocarbon cracking. Therefore,
518 pore pressure can be estimated from formation porosity. Fig. 9 illustrates how to identify under-
519 compaction and overpressure from porosity profile. When the porosity is reversal, the under-compaction
520 occurs and overpressure generates. The starting point of the porosity reversal is the top of under-
521 compaction or top of overpressure. In the formation with under-compaction, porosity and pore pressure
522 are higher than those in the normally compacted one.

523 Efforts have been made to use porosity data for predicting pore pressure in shales and mudstones.
524 For instance, Holbrook et al. (2005) presented porosity-dependent effective stress for pore pressure
525 prediction. Heppard et al. (1998) used an empirical porosity equation similar to Eaton's sonic method to
526 predict pore pressure using shale porosity data. Flemings et al. (2002) and Schneider et al. (2009) also
527 applied porosity-stress relationships to predict overpressures in mudstones.

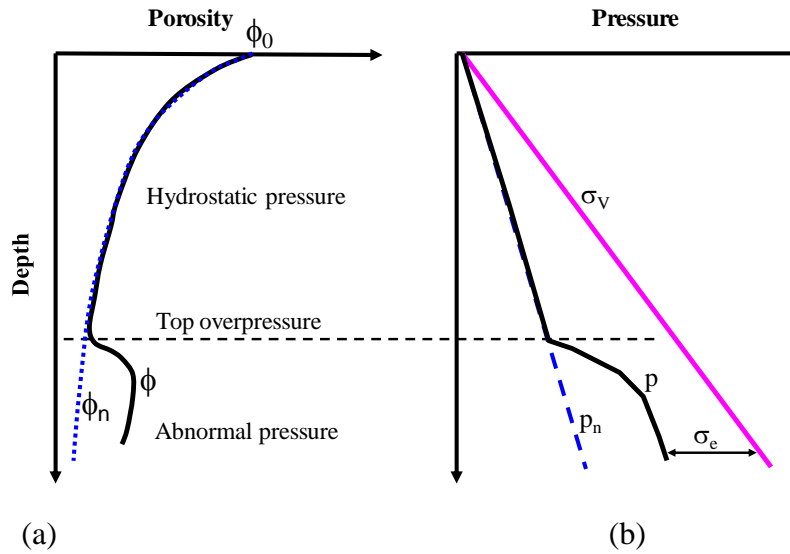


Fig. 9. Schematic porosity (a) and corresponding pore pressure (b) in a sedimentary basin. The dash porosity profile in (a) represents normally compacted formation. In the overpressured section the porosity reversal occurs (heavy line). In the overpressured section, porosity is larger than that in the normal compaction trendline (ϕ_n).

The author derived a theoretical equation for pore pressure prediction from porosity according to normal compaction trend of porosity (Zhang 2008). The pore pressure gradient can be calculated from the following equation (refer to Appendix A for derivations):

$$P_{pg} = OBG - (OBG - P_{ng}) \frac{\ln \phi_0 - \ln \phi}{cZ} \quad (26)$$

where ϕ is the porosity in shale at depth of Z , can be obtained from sonic or density logs, ϕ_0 is the porosity in the mudline (in the ground surface or sea floor); Z is the depth below the mudline; c can be obtained from the normal compaction porosity trendline in Eq. 28.

From Eq. 26 the pore pressure, overburden stress and porosity have the following relationship:

$$p = \sigma_v - (\sigma_v - p_n) \frac{\ln \phi_0 - \ln \phi}{cZ} \quad (27)$$

The primary difference between Eq. 27 and other existing pore pressure-porosity equations is that the pressures calculated from Eq. 27 are dependent on depths. In other words, the normal compaction trendline of porosity is not a constant, but a function of depth.

When porosity (ϕ) at an interested depth is greater than the normal porosity (ϕ_n) at the same depth, the formation has overpressure. The normal compaction porosity trendline can be determined from the following equation (rewritten from Eq. 24):

$$\phi_n = \phi_0 e^{-cZ} \quad (28)$$

4.2. Pore pressure prediction from transit time or velocity

Porosity (ϕ) in Eqs. 26 and 27 can be obtained from density and sonic logs or from seismic interval velocity. The following equation represents one of the methods to calculate porosity from compressional velocity/transit time proposed by Raiga-Clemenceau et al. (1988):

$$\phi = 1 - \left(\frac{\Delta t_m}{\Delta t} \right)^{\frac{1}{x}} \quad (29)$$

where x is the exponent to be determined from the data. In a study of compaction in siliciclastic rocks, predominantly shales, in the Mackenzie Delta of northern Canada, Issler (1992) obtained laboratory measurements of porosity in shales and determined a value of 2.19 for the exponent x and used a fixed value of shale transit time, $\Delta t_m = 67 \mu\text{s/ft}$.

Substituting Eq. 29 into Eq. 26, the pore pressure can be predicted from the compressional transit time/velocity, i.e.:

$$P_{pg} = OBG - (OBG - P_{ng}) \frac{C_m - \ln[1 - (\Delta t_m / \Delta t)^{1/x}]}{cZ} \quad (30)$$

where C_m is the constant related to the compressional transit time in the matrix and the transit time in the mudline, and $C_m = \ln[1 - (\Delta t_m / \Delta t_{ml})^{1/x}]$.

Porosity is often estimated by the empirical time average equation presented by Wyllie et al. (1956):

$$\phi = \frac{\Delta t - \Delta t_m}{\Delta t_f - \Delta t_m} \quad (31)$$

where Δt_f is the transit time of interstitial fluids.

Substituting Wyllie's porosity-transit time equation into Eqs. 26 and 27, we obtain the following equations to calculate pore pressure gradient (P_{pg}) and pore pressure (p):

$$P_{pg} = OBG - (OBG - P_{ng}) \frac{\ln(\Delta t_{ml} - \Delta t_m) - \ln(\Delta t - \Delta t_m)}{cZ} \quad (32)$$

$$p = \sigma_v - (\sigma_v - p_n) \frac{\ln(\Delta t_{ml} - \Delta t_m) - \ln(\Delta t - \Delta t_m)}{cZ} \quad (33)$$

The normal compaction trendline of the transit time in Eqs. 32 and 33 can be obtained from the following equation (refer to Appendix B for derivations):

$$\Delta t_n = \Delta t_m + (\Delta t_{ml} - \Delta t_m)e^{-cZ} \quad (34)$$

This normal compaction trend allows the normal transit time to approach the matrix transit time at a very large depth, which is physically correct as Chapman (1983) pointed out. Unlike other methods, this proposed sonic method (Eqs. 32, 33) uses a normal compaction trendline that is asymptotic to matrix transit time and therefore better represents the compaction mechanism of the sediments. The other advantage of this model is that the calculated pore pressures are dependent on depth, and both effects of the matrix and mudline transit time are considered.

4.3. Case applications

The proposed methods (porosity model in Eqs. 26, 27, and velocity model in Eqs. 32, 33) have been applied in several petroleum basins (e.g., in the Gulf of Mexico, North Sea and onshore conventional gas and shale gas formations) to verify the applicability. Three examples of deepwater wells in the Gulf of Mexico are presented in the following section.

4.3.1. Pore pressure from porosity model

The same case study as shown in Figs. 6 and 8 is used in this section for the comparison purpose. An important step in performing pore pressure analysis is to select the clean shales in well log data. Prior to applying the porosity model, one needs to obtain the shale porosity from density log or sonic log. Clay minerals have a crystalline structure that can contain more radioactive elements than sandstones. Therefore, gamma ray data in well logs can be used to differentiate shale intervals from those of other lithologies. Drawing shale base lines in gamma ray data are the first step to identify and separate shale from other rocks, as shown in Fig. 10. The high gamma ray values (>75-110 API) are assumed to be pure shale, whereas points where gamma ray values are less than the shale base lines are not used for analysis. Shale points defined on the gamma ray log are then transferred to the corresponding sonic log or other logs used for pore pressure analysis (KSI, 2001).

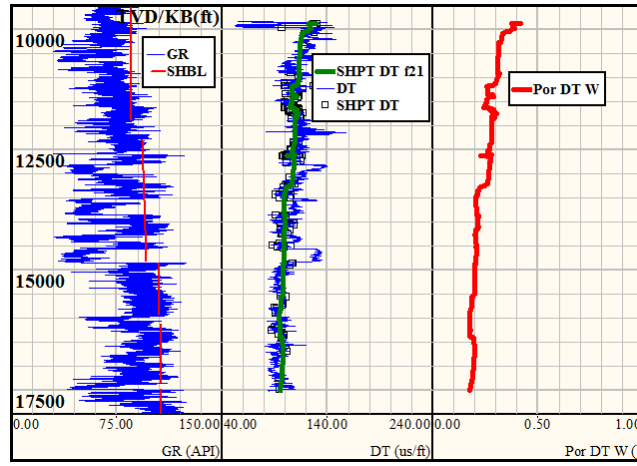


Fig. 10. Log data and the calculated porosity from sonic transit time by Wyllie's equation (Eq. 31) in a deepwater well of the Gulf of Mexico. In this figure, the gamma ray and shale base lines (SHBL) are shown in the left track; the sonic transit time (DT), shale points of the transit time (SHPT DT), and filtered shale transit time in shale (SHPT DT f21) are plotted in the second track; and the calculated porosity from the filtered shale transit time is shown in the right track.

Fig. 10 demonstrates how to obtain shale porosity from gamma ray and sonic logs. Porosity is calculated from the shale transit time from Wyllie's equation (Eq. 31) using $\Delta t_f = 200 \mu\text{s/ft}$ and $\Delta t_m = 70 \mu\text{s/ft}$. Using this porosity data, the normal compaction trend in porosity is analyzed based on Eq. 28 with the parameters of $\phi_0 = 0.8$ and $c = 0.00024$, as shown in Figs. 9.a and 11.a. Then, pore pressure gradient is calculated from the porosity model (Eq. 26) with parameters obtained from Fig. 11.a ($\phi_0 = 0.8$, $c = 0.00024$) and $P_{ng} = 8.7 \text{ ppg}$. The calculated pore pressure gradient is compared to the measured pore pressure from the repeat formation tests (RFT) and mud weight, as shown in Fig. 11.b. Compared to the pore pressure obtained from the modified Eaton's sonic method (Fig. 8.b), the proposed porosity method (as shown in Fig. 11.b) gives a much better result in terms of matching measured pore pressures.

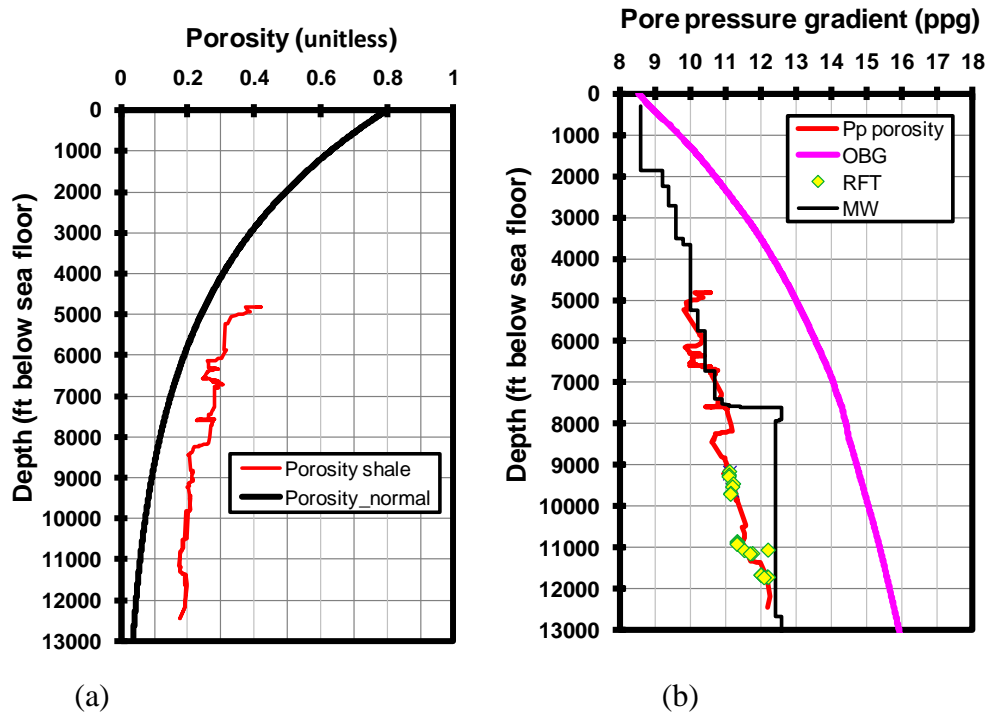


Fig. 11. Pore pressure prediction from the porosity method (Eq. 26) using the data shown in Fig. 8. The left track presents porosity of shales obtained from Fig. 10 and normal compaction trendline of porosity calculated from Eq. 28. The right track plots overburden stress gradient (OBG), mud weight used while drilling (MW), measured pore pressure (RFT), and pore pressure profile calculated from the porosity by Eq. 26 (Pp porosity).

4.3.2. Pore pressure from sonic transit time model

This case study presents another post-drill pore pressure analysis in a Gulf of Mexico deepwater oil field with water depth of 3850 ft. The formations are Tertiary shales and sandstones, and the target zone is located in the Middle Miocene sandstones. Fig. 12 shows a post-drill pore pressure analysis to examine the proposed sonic model. Pore pressure gradient is calculated from proposed sonic equation (Eq. 32) using $\Delta t_{ml} = 200 \mu\text{s}/\text{ft}$ and $\Delta t_m = 70 \mu\text{s}/\text{ft}$, $P_{ng} = 8.75 \text{ ppg}$, and $c = 0.00028$. The pore pressure gradient is also estimated using Bowers' method (Eq. 9) with $\Delta t_{ml} = 200 \mu\text{s}/\text{ft}$, $P_{ng} = 8.75 \text{ ppg}$, $A = 14$, $B = 0.745$. Compared to the result obtained from Bowers' method, the proposed method (Eq. 32) gives a better result in pore pressure calculation, particularly in the shallow section, where other sonic methods overestimate the pore pressures.

The proposed sonic method uses a normal compaction trendline and the calculated pressures are dependent on depth. Therefore, the pore pressures in both shallow and deep depths can be better predicted.

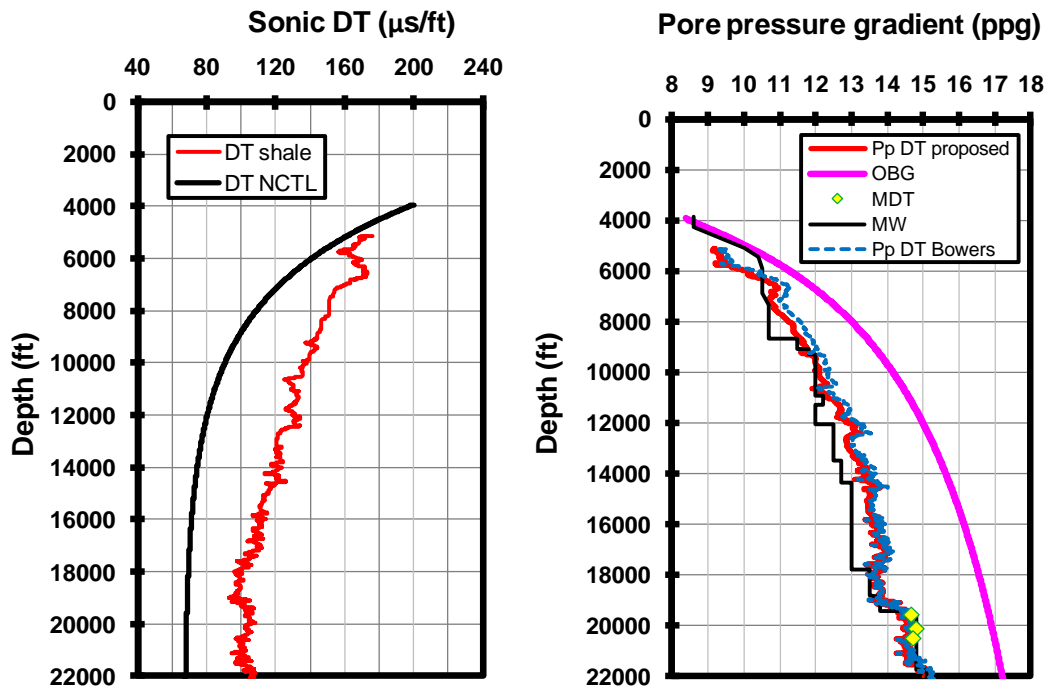


Fig. 12. Pore pressure calculations from the sonic transit time method proposed in this paper (Eq. 32) and from Bower's method. The left track presents the transit time of shales obtained from sonic log and normal compaction trendline of transit time calculated from Eq. 34. The right track plots overburden stress gradient, mud weight used while drilling, measured pore pressure from MDT, and pore pressure profile calculated from the transit time by Eq. 32 and by Bower's method.

4.3.3. Pore pressure from sonic transit time model in subsalt formations

Pore pressure prediction is very challenging in subsalt formations because the formations may be affected by salt with high salinity, thus a much lower resistivity. In addition, the salt tectonics may affect the formation compaction status, causing normal compaction trend changes. Furthermore, the surface seismic survey cannot provide reliable interval velocities in the subsalt formations. Therefore, sonic log is critically important for pore pressure prediction while drilling. We examine a borehole drilled in a deepwater subsalt formations of the Gulf of Mexico. The field description can be found in Zhang et al. (2008). Pore pressure gradient is calculated from the proposed sonic equation (Eq. 32) using $\Delta t_{ml} = 120$ $\mu\text{s/ft}$ and $\Delta t_m = 73$ $\mu\text{s/ft}$, $P_{ng} = 8.75$ ppg and $c = 0.00009$. Compared to the measured formation pressures, the proposed method (Eq. 32) gives an excellent pore pressure calculation in subsalt formations, as shown in Fig. 13. It should be noted that the mudline transit time needs to be adjusted ($\Delta t_{ml} = 120$ $\mu\text{s/ft}$, instead of 200 $\mu\text{s/ft}$ in conventional cases) to make a better pore pressure estimation in subsalt formation.

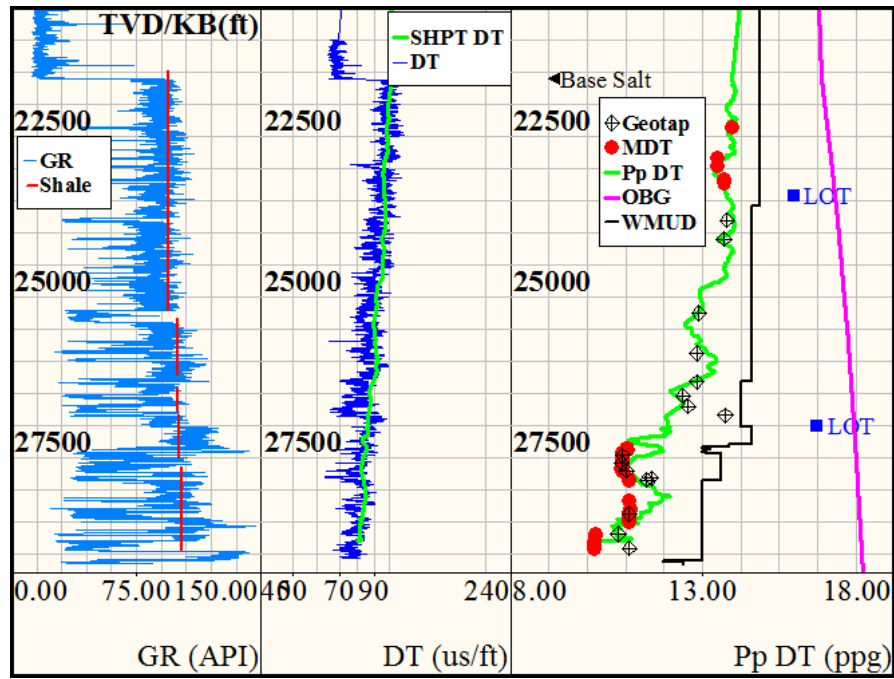


Fig. 13. Pore pressure calculation from the sonic transit time proposed in this paper (Eq. 32) in deepwater subsalt formations of the Gulf of Mexico. In this figure, the gamma ray and shale base lines are shown in the left track; the sonic transit time (DT) and filtered shale points of the transit time (SHPT DT) are plotted in the second track; and the calculated pore pressure from the filtered shale transit time (Pp DT) is shown in the right track with comparison to the measured formation pressures (MDT and Geotap).

5. Conclusions

For a hydraulically-connected/permeable aquifer or hydrocarbon-bearing formation (e.g., sandstone, limestone), the formation pore pressure at the target depth can be calculated based on the difference of the fluid column at the other depth where the pressure is known. However, in the formations of shales the pore pressures are overpressured in the deep regions and the shales may not be hydraulically connected. The pore pressures in shales cannot be easily obtained from the fluid flow theory, because the overpressures are primarily caused by compaction disequilibrium. Instead, well log or shale petrophysical data can be used to estimate the pore pressures in shales. Eaton's resistivity and sonic methods are adapted to provide a much easier way to handle normal compaction trendlines. Theoretical pore pressure-porosity model is the fundamental for pore pressure prediction in shales, where the compaction disequilibrium is the primary mechanism of overpressure generation. Using this theoretical model, pore pressure prediction from porosity and compressional velocity (sonic transit time) have been obtained. Case studies show that pore pressures can be accurately obtained from well logging data using correct methods with necessary calibrations.

680
681
682

Appendix A: Derivation of pore pressure prediction from porosity

683 It is well known that the formation porosity and effective stress have the following relationship:

$$684 \quad \phi = \phi_0 e^{-a\sigma_e} \quad (A1)$$

685 Therefore, the effective stress can be obtained from Eq. A1:

$$686 \quad \sigma_e = \frac{1}{a} \ln \frac{\phi_0}{\phi} \quad (A2)$$

687 The effective stress at normal pressure condition can also be obtained from Eq. A1, when the porosity is
688 the normal porosity, a condition that formations are normally compacted, i.e.:

$$689 \quad \phi_n = \phi_0 e^{-a\sigma_n} \quad (A3)$$

$$690 \quad \sigma_n = \frac{1}{a} \ln \frac{\phi_0}{\phi_n} \quad (A4)$$

691 Combining Eqs. A2 and A4, one has:

$$692 \quad \frac{\sigma_e}{\sigma_n} = \frac{\ln \phi_0 - \ln \phi}{\ln \phi_0 - \ln \phi_n} \quad (A5)$$

693 Or,

$$694 \quad \sigma_e = \sigma_n \frac{\ln \phi_0 - \ln \phi}{\ln \phi_0 - \ln \phi_n} \quad (A6)$$

695 If we assume the Biot coefficient $\alpha = 1$ in Eq. 1, then, the effective stress and pore pressure have the
696 following relationship:

$$697 \quad p = \sigma_v - \sigma_e \quad (A7)$$

698 Substituting Eq. A6 into Eq. A7 and noticing $\sigma_n = \sigma_v - p_n$, we can obtain pore pressure, overburden
699 stress and porosity relationship:

$$700 \quad p = \sigma_v - (\sigma_v - p_n) \frac{\ln \phi_0 - \ln \phi}{\ln \phi_0 - \ln \phi_n} \quad (A8)$$

701 where ϕ_n is the porosity in the condition of the formation with a normal compaction.

702 The normal compaction porosity can be obtained from the following equation (Eq. 24):

$$703 \quad \phi_n = \phi_0 e^{-cZ} \quad (A9)$$

704 Substituting Eq. A9 into Eq. A8, we obtain the pore pressure and porosity relationship:

$$705 \quad p = \sigma_v - (\sigma_v - p_n) \frac{\ln \phi_0 - \ln \phi}{cZ} \quad (A10)$$

where p is the pore pressure; σ_v is the overburden stress; p_n is the normal pore pressure; ϕ is porosity in shale, ϕ_0 is the porosity in the mudline (the ground surface or sea floor); Z is the depth below the mudline; and c is the constant.

The pore pressure gradient can be easily obtained from Eq. A10.

$$P_{pg} = OBG - (OBG - P_{ng}) \frac{\ln \phi_0 - \ln \phi}{cZ} \quad (A11)$$

where P_{pg} is the pore pressure gradient; OBG is the overburden stress gradient; P_{ng} is the normal pressure gradient.

Appendix B: Derivation of sonic normal compaction equation

From Wyllie equation (i.e., Eq. 31), the porosity at normal compaction condition (ϕ_n) can be expressed as:

$$\phi_n = \frac{\Delta t_n - \Delta t_m}{\Delta t_f - \Delta t_m} \quad (B1)$$

And the porosity in the mudline (ϕ_{ml}) can be written as follows:

$$\phi_{ml} = \frac{\Delta t_{ml} - \Delta t_m}{\Delta t_f - \Delta t_m} \quad (B2)$$

From Eq. A9, we have the following relationship between the normal porosity and mudline porosity:

$$\phi_n = \phi_{ml} e^{-cZ} \quad (B3)$$

Substituting Eqs. B1 and B2 into Eq. B3, we can obtain the transit time in the normal compaction trend, i.e.:

$$\Delta t_n = \Delta t_m + (\Delta t_{ml} - \Delta t_m) e^{-cZ} \quad (B4)$$

References

- Athy, L. F., 1930. Density, porosity, and compaction of sedimentary rocks: AAPG Bulletin, 14 (1):1-24.
- Biot, M.A., 1941. General theory of three-dimensional consolidation. J. Appl. Phys. 12(1):155-164.
- Bowers, G. L., 1995. Pore pressure estimation from velocity data; accounting for overpressure mechanisms besides undercompaction. SPE Drilling and Completions, June, 1995:89-95.
- Bowers, G. L., 2001. Determining an Appropriate Pore-Pressure Estimation Strategy, Paper OTC 13042.
- Burrus, J., 1998, Overpressure models for clastic rocks, their relation to hydrocarbon expulsion: a critical reevaluation. In Law, B.E., G.F. Ulmishek, and V.I. Slavin eds., Abnormal pressures in hydrocarbon environments: AAPG Memoir 70, p. 35–63.
- Chapman, R.E., 1983. Petroleum geology. Elsevier.

736 Daines, S.R., 1982. Prediction of fracture pressures for wildcat wells. JPT 34:863-872.

737 Davies, R. J., Swarbrick, R.E., Evans, R.J., Huuse, M., 2007. Birth of a mud volcano: East Java, 29 May
738 2006. GSA Today, 17(2), doi: 10.1130/GSAT01702A.1.

739 Dickinson, G., 1953. Geological aspects of abnormal reservoir pressures in Gulf Coast Louisiana: AAPG
740 Bulletin, 37(2):410-432.

741 Dodson, J.K., 2004. Gulf of Mexico ‘trouble time’ creates major drilling expenses. Offshore, 64(1).

742 Dutta, N.C., 2002. Geopressure prediction using seismic data: Current status and the road ahead.
743 Geophysics, 67(6):2012–2041.

744 Eaton, B.A., 1968. Fracture gradient prediction and its application in oilfield operations. Paper SPE2163.
745 JPT, p25-32.

746 Eaton, B.A., 1972. The effect of overburden stress on geopressures prediction from well logs. Paper
747 SPE3719. JPT, Aug., 1972:929-934.

748 Eaton, B. A., 1975. The equation for geopressure prediction from well logs. Society of Petroleum
749 Engineers of AIME, paper SPE 5544.

750 Flemings, P.B., Stump B.B., Finkbeiner, T., Zoback, M. 2002. Flow focusing in overpressured
751 sandstones: theory, observations, and applications. American J. of Science, 302:827–855.

752 Gardner, G.H.F., Gardner, L.W. and Gregory, A.R. (1974), Formation Velocity and Density – the
753 Diagnostic Basis for Stratigraphic Traps, Geophysics, Vol 39, No 6, pp.2085-2095.

754 Gutierrez, M.A., Braunsdorf, N.R., Couzens, B.A., 2006. Calibration and ranking of pore-pressure
755 prediction models. The leading Edge, Dec., 2006:1516-1523.

756 Haimson, B.,C., Fairhurst, C., 1970. In situ stress determination at great depth by means of hydraulic
757 fracturing. Rock Mechanics - Theory and Practice, Somerton W.H. (ed). Am. Inst. Mining. Eng.
758 pp559-584

759 Heppard, P.D., Cander, H.S., Eggertson, E.B., 1998, Abnormal pressure and the occurrence of
760 hydrocarbons in offshore eastern Trinidad, West Indies, in Law, B.E., G.F. Ulmishek, and V.I. Slavin
761 eds., Abnormal pressures in hydrocarbon environments: AAPG Memoir 70, p. 215–246.

762 Holbrook, P.W., Maggiori, D.A., Hensley, R., 2005. Real-time pore pressure and fracture gradient
763 evaluation in all sedimentary lithologies, SPE Formation Evaluation, 10(4):215-222.

764 Holand P., Skalle, P., 2001. Deepwater Kicks and BOP Performance. SINTEF Report for U.S. Minerals
765 Management Service.

766 Hottmann, C.E., Johnson, R.K., 1965. Estimation of formation pressures from log-derived shale
767 properties. Paper SPE1110, JPT, 17:717-722.

768 Hubbert, M.K., Willis, D.G., 1957. Mechanics of hydraulic fracturing. Pet. Trans. AIME., 210:153-163.

769 Issler, D.R., 1992. A new approach to shale compaction and stratigraphic restoration, Beaufort-Mackenzie
770 Basin and Mackenzie Corridor, Northern Canada. AAPG Bulletin, 76:1170-1189.

771 KSI, 2001. Best practice procedures for predicting pre-drill geopressures in deep water Gulf of Mexico.
772 DEA Project 119 Report, Knowledge Systems Inc.

773 Lang, J., Li, S., Zhang, J., 2011. Wellbore stability modeling and real-time surveillance for deepwater
774 drilling to weak bedding planes and depleted reservoirs. SPE/IADC 139708.

775 Law, B.E., and C.W. Spencer, 1998, Abnormal pressures in hydrocarbon environments, in Law, B.E.,
776 G.F. Ulmishek, and V.I. Slavin eds., Abnormal pressures in hydrocarbon environments: AAPG
777 Memoir 70, p.1–11.

778 Lopez, J.L., Rappold, P.M., Ugueto, G.A., Wieseneck, J.B., Vu, K., 2004. Integrated shared earth model:
779 3D pore-pressure prediction and uncertainty analysis. The leading Edge, Jan., 2004:52-59.

780 Matthews, W.R., Kelly, J., 1967. How to predict formation pressure and fracture gradient. Oil Gas J.
781 65:92-106.

782 Meng, Z., Zhang, J., Wang, R., 2011. In-situ stress, pore pressure and stress-dependent permeability in the
783 Southern Qinshui Basin. Int. J. Rock Mech. Min. Sci., 48(1):122-131.

784 Morley, C.K., King, R., Hillis, R., Tingay, M., Backe, G., 2011. Deepwater fold and thrust belt
785 classification, tectonics, structure and hydrocarbon prospectivity: A review. Earth-Science Reviews,
786 104: 41–91.

787 Mouchet, J.-C., Mitchell, A., 1989. Abnormal pressures while drilling. Editions TECHNIP, Paris.

788 Nelson, H.N., Bird, K.J., 2005. Porosity-depth trends and regional uplift calculated from sonic logs,
789 National Reserve in Alaska. Scientific Investigation Report 2005-5051, U.S. Dept. of the Interior and
790 USGS.

791 Peng, S., Zhang, J., 2007. Engineering geology for underground rocks. Springer.

792 Powley, D.E., 1990. Pressures and hydrogeology in petroleum basins. Earth-Sci. Rev., 29: 215-226.

793 Raiga-Clemenceau, J., Martin, J.P., and Nicoletis, S., 1988. The concept of acoustic formation factor for
794 more accurate porosity determination from sonic transit time data. Log Analyst, 29(1):54–60.

795 van Ruth, P., Hillis R., Tingate, P., 2004. The origin of overpressure in the Carnarvon Basin, Western
796 Australia: implications for pore pressure prediction. Petroleum Geoscience, 10:247–257.

797 Sayers, C.M., Johnson, G.M. and Denyer, G., 2002. Predrill pore pressure prediction using seismic data.
798 Geophysics, 67: 1286-1292.

799 Schneider, J., Flemings, P.B., Dugan, B., Long, H., Germaine, J.T., 2009. Overpressure and consolidation
800 near the seafloor of Brazos-Trinity Basin IV, northwest deepwater Gulf of Mexico. J. Geophys. Res.,
801 114, B05102,

802 Slotnick, M.M., 1936. On seismic computation with applications. *Geophysics*, 1: 9-22.

803 Skalle, P., Podio, A.L., 1998. Trends extracted from 1,200 Gulf Coast blowouts during 1960-1996. *World*
804 *Oil*, June, 1998:67-72.

805 Swarbrick, R.E., Osborne, M.J., 1998, Mechanisms that generate abnormal pressures: an overview, in
806 Law, B.E., G.F. Ulmishek, and V.I. Slavin eds., *Abnormal pressures in hydrocarbon environments*:
807 AAPG Memoir 70, p. 13–34.

808 Swarbrick, R.E., Osborne, M.J., Yardley, G.S., 2002, Comparison of overpressure magnitude resulting
809 from the main generating mechanisms, in A. R. Huffman and G. L. Bowers, eds., *Pressure regimes in*
810 *sedimentary basins and their prediction*: AAPG Memoir 76, p. 1–12.

811 Terzaghi, K., Peck, R.B., Mesri, G., 1996. *Soil Mechanics in Engineering Practice* (3rd Edition). John
812 Wiley & Sons.

813 Tingay, M.R.P., Hillis, R.R., Swarbrick, R.E., Morley, C.K. Damit, A.R., 2009. Origin of overpressure
814 and pore-pressure prediction in the Baram province, Brunei. *AAPG Bulletin*, 93(1):51–74.

815 Traugott, M., 1997. Pore pressure and fracture gradient determinations in deepwater. *World Oil*, August,
816 1997.

817 Wyllie, M.R.J., Gregory, A.R., Gardner, L.W., 1956. Elastic wave velocities in heterogeneous and porous
818 media. *Geophysics*, 21:41-70.

819 Yardley, G.S., Swarbrick, R.E., 2000. Lateral transfer: a source of additional overpressure? *Marine and*
820 *Petroleum Geology* 17, 523-537.

821 York, P., Prithard, D., Dodson, J.K., Dodson, T., Rosenberg, S., Gala, D., Utama, B., 2009. Eliminating
822 non-productive time associated drilling trouble zone. OTC20220 presented at the 2009 Offshore Tech.
823 Conf. held in Houston.

824 Zhang, J., Roegiers, J.-C., 2005. Double porosity finite element method for borehole modeling.
825 *Rock Mech. Rock Engng.* 38, 217–242.

826 Zhang, J., 2008. Unpublished reports and training notes.

827 Zhang, J., Standifird, W.B., Lenamond, C., 2008. Casing Ultradeep, Ultralong Salt Sections in Deep
828 Water: A Case Study for Failure Diagnosis and Risk Mitigation in Record-Depth Well, Paper SPE
829 114273.

830 Zhang, J., Roegiers, J.-C., 2010. Discussion on “Integrating borehole-breakout dimensions, strength
831 criteria, and leak-off test results, to constrain the state of stress across the Chelungpu Fault, Taiwan”.
832 *Tectonophysics*, 492, 295-298.